Pattern formation in a vibrated granular layer: The pattern selection issue

E. Clément and L. Labous
Laboratoire des Milieux Désordonnés et Hétérogènes, CNRS UMR No. 7603, Université Pierre et Marie Curie, Boîte Postale 86, 4 Place Jussieu, F-75252 Paris, France
(Received 26 April 2000)

We present a numerical study of a surface instability occurring in a bidimensional vibrated granular layer. The driving mechanism for the formation of stationary waves is closely followed. Two regimes of wavelength selection are identified: a dispersive regime where the wavelength decreases with increasing frequency and a saturation regime where the value of the wavelength is a constant depending on the number of grains in the vertical direction. For the dispersive regime an empirical relation is proposed, based on dimensional arguments involving transport properties in the layer. A comparison is made with existing experimental results in two and three dimensions. For the saturation regime, a connection is established between the pattern formation and an intrinsic instability occurring spontaneously in dissipative gases. The observed dependence on the layer height is linked to a detailed dissipation mechanism for the collisions between grains.

PACS number(s): 45.70.Qj, 81.05.Rm

I. INTRODUCTION

Granular assemblies under vertical vibrations show a very broad and interesting phenomenology. They have been studied from various different viewpoints experimentally, numerically, or theoretically (for extensive reviews on the subject see [1,2] and references therein). In a series of experiments Melo, Ubanhovar, and Swinney [3] reported a pattern-forming instability occurring in a layer of grains vibrating on a plate (see also [4]). This phenomenon is the three-dimensional (3D) version of a surface instability first reported by Fauve, Douady, and Laroche [5] in a small rectangular cell containing sand. The phenomenology of the 3D patterns (squares, stripes, hexagons) is strongly reminiscent of the outcome for a parametric instability occurring in vibrated fluid layers called the Faraday instability [6] (see Ref. [7] for a modern viewpoint and references). The pattern phenomenology exhibits interesting features such as localized excitation (the so-called oscillons) [8] as well as skew-varicose patterns [9]. Experiments showing surface patterns were also performed on 2D granular layers confined in a 2D cell [10]. The dispersion relation of the excited standing waves was related quantitatively to the dispersion relation observed in 3D. In a first approximation, the phenomenon is a parametric resonance occurring at a time scale corresponding to gravity restoring mechanisms of the layer deformations. Numerical simulations were performed using an event-driven algorithm in a 2D geometry [11], and in 3D [12] also using a soft-particle algorithm [13] qualitatively reproducing the phenomenon. Recent simulations of a simplified toy model for horizontal momentum transfer also reproduce the pattern formation [14] and in some limit the dispersion relation. Various theoretical models have been proposed to describe the pattern-forming instability [15–19] but, although displaying a close pattern phenomenology, they do not give the proper measured dispersion relation. Basically, the horizontal momentum transfer is accounted for phenomenologically with a diffusive term. This provides a selected wavelength decreasing like the inverse square root of the frequency instead of, roughly, like the inverse of the frequency squared for a ''pure'' gravity restoring mechanism. An exception may be made for the article by Eggers and Riecke [19], who really tried to fit some of the experimental results. But in this article the momentum transfer relation was designed in an *ad hoc* manner to agree with the experimental dispersion relation. In fact, what is observed is not exactly the gravity dependence; experimental and simulation data were taken in a domain where the layer height is still comparable with the wavelength size and thus internal motion might still play a role. Nevertheless, there are strong pieces of evidence that in the low frequency limit pure gravity wave behavior should be found. The diffusive ansatz may not be crucial to understanding the issue of pattern formation (square, stripe, hexagon, etc.) but as far as mass, momentum, and energy transfer mechanisms are concerned it is likely that it is not the proper physical mechanism. Recently, starting from a set of continuum equations describing granular gases, Bizon, Shattuck, and Swift [20] found a pattern selection mechanism for an isothermal and incompressible fluid with an effective viscosity also designed to fit the data. Finally, a recent report was made on a large series of experimental measurements addressing the issue of wavelength selection in 3D. Propositions were made to link the observed wavelength to the mobility properties of the grains [21].

In our opinion, in spite of those many different approaches, there is still no full understanding of the basic mechanisms driving this instability. The fundamental aspects of energy, mass, and momentum transfers are still ill understood. In this paper we present an extensive study of 2D numerical simulations of dissipative grains which aims to investigate in detail the various mechanisms leading to wavelength selection. We use an optimized version of an event-driven algorithm already presented by Luding *et al.* [11]. We propose here a view slightly different from previous ones and we give evidence for a mechanism of pattern selection. Preliminary results on this issue were already presented elsewhere [22].

II. NUMERICAL SIMULATION

The system we investigate consists of N beads in a container of size L, constrained to move in 2D. The bottom plate

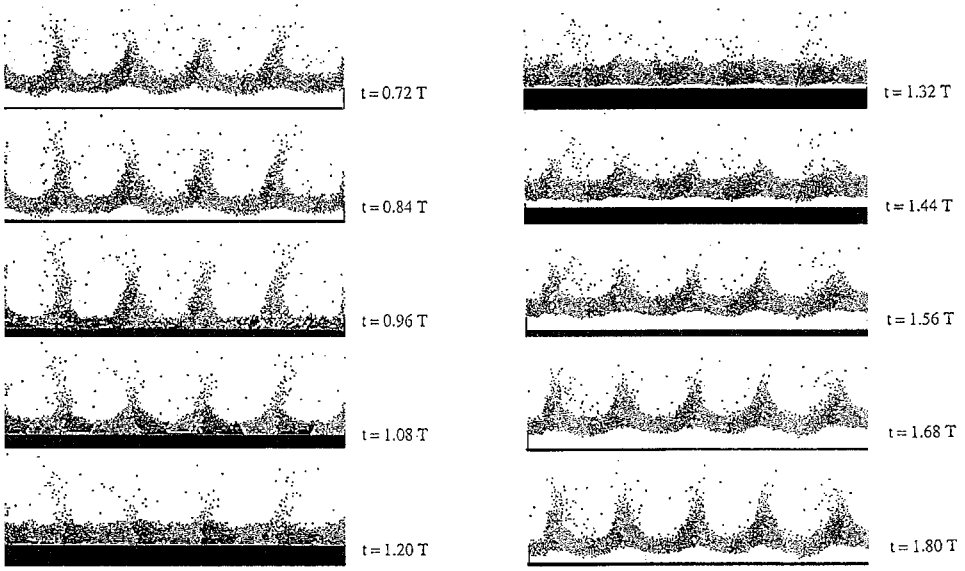

FIG. 1. Display of the vibrated layer during two vibration periods. Black particles have a horizontal velocity to the right and gray ones to the left. The simulation parameters are $N_h = 12$, $f = 15$ Hz, $d = 1$ mm, and $\Gamma = 3.6$.

moves vertically with a trajectory $z(t) = a \sin \omega t$ [a is the amplitude and $f = \omega/2\pi$ the frequency]. The boundary conditions are *periodic*. Our simulation principle is based on the so-called event-driven method, which is suited for hard spheres only. As a consequence, we have no explicit interaction potential. The interaction rules are provided in a collision matrix which tells us, for each collision, what happens to the rotation and translation velocities after the collision as a function of rotation and translation velocities before the shock. This is a very efficient method in a situation where the dynamics can be decomposed into sequences of binary collisions. The collision interactions stem from a collision matrix described in Ref. [11] whose physical foundations can be found in Refs. [23,24]. The collision parameters are a frontal restitution ε coefficient, a tangential restitution coefficient β (with a maximal value β_0), and a friction coefficient μ. To avoid as much as possible the so-called inelastic collapse [25], the frontal restitution coefficient is taken to decrease with velocity:

$$\varepsilon(u) = 1 - \varepsilon_0 \left(\frac{u}{u^*} \right)^{1/5} \tag{1}$$

with u the relative velocity in the normal direction and $u^* = 1$ m/s. This is the so-called Herz-Kuwabara-Kono model [26]. A dissipation cutoff is introduced for small impact velocities (for $u < u_0 = 10^{-6}\,\mathrm{m\,s^{-1}}$ we set $\varepsilon = 1$). The importance and the influence of this ''trick'' to avoid inelastic collapse was investigated in detail by Luding and McNamara [27]. The N spheres of diameter d are initially packed in the cells with horizontal width L; the layer thickness is defined as $H = \sqrt{\frac{3}{2}}\, N_h d$. The algorithm efficiency is improved by implementation of a time delay procedure applied to the search of the event sequence [28]. Such a procedure increases the computing time as $O(N \log N)$ instead of $O(N^2)$ for a standard event-driven algorithm [11]. The simulations can handle system sizes as large as $N = O(10^5)$ particles. Typically we use $\varepsilon_0 = 0.4$ (for bead-plate collisions, this coefficient is set equal to 0). The other physical parameters are $\beta_0 = 0.0$ and $\mu = 0.2$. This choice was made to get as close as possible to the aluminum bead values used in the experiment of Clément *et al.* [10], i.e., for typical impact velocities $U = 1$ m/s, we have $\varepsilon = 0.6$. Also, we checked that this parameter choice (β_0 and μ) is noncritical as long as there is (i) enough dissipation to avoid fluidization of the layer [29], (ii) a dissipation cutoff to avoid inelastic collapse [25], and (iii) some friction between the beads and with the bottom plate, in order to stabilize the patterns.

III. PATTERN PHENOMENOLOGY

For a relative acceleration $\Gamma = a\omega^2/g$ situated in a moderate range beyond the threshold $\Gamma \simeq 2.5$ up to $\Gamma = 4$, an instability occurs and a stationary pattern is obtained with a wavelength λ roughly constant (within a few percent). The pattern is made of peaks such that minima and maxima exchange positions at each period of excitation (see Fig. 1). The impact frequency corresponds to the vibration frequency and the layer response is then at $\omega_0 = \omega/2$. The instability stops for values of the acceleration around $\Gamma = 4.2$; this is due to a well known problem of matching between the downward velocity of the plate and the velocity of the falling layer (see the discussion on this effect and references in [2]). The instability is resumed for larger accelerations (around $\Gamma = 6$) but with a free flight of the layer lasting twice the excitation period; the layer response is then $\omega_0 = \omega/4$. As already noticed in Refs. [3] and [10], two important phases of the layer response can be considered: the free flight phase (lasting about $1/2f$) where the peak pattern is forming, and the energy input phase, where the plate is in contact with the layer and provides energy into the system. In general, the peak zone collides at a phase slightly delayed with respect to the minimum zone. This is due to the general presence of an arch at the bottom of the layer as already observed experimentally [10] and numerically [11].

In Fig. 2, we represent the pressure and density fields superposed for two different frequencies. Spatial distortion of the layer as well as internal compression and dilation waves are evident in this plot. We also observe that the peak wavelength, the bottom arch amplitude, and the peak amplitude decrease as the frequency is increased.

In Fig. 3, we display a spatiotemporal diagram of the

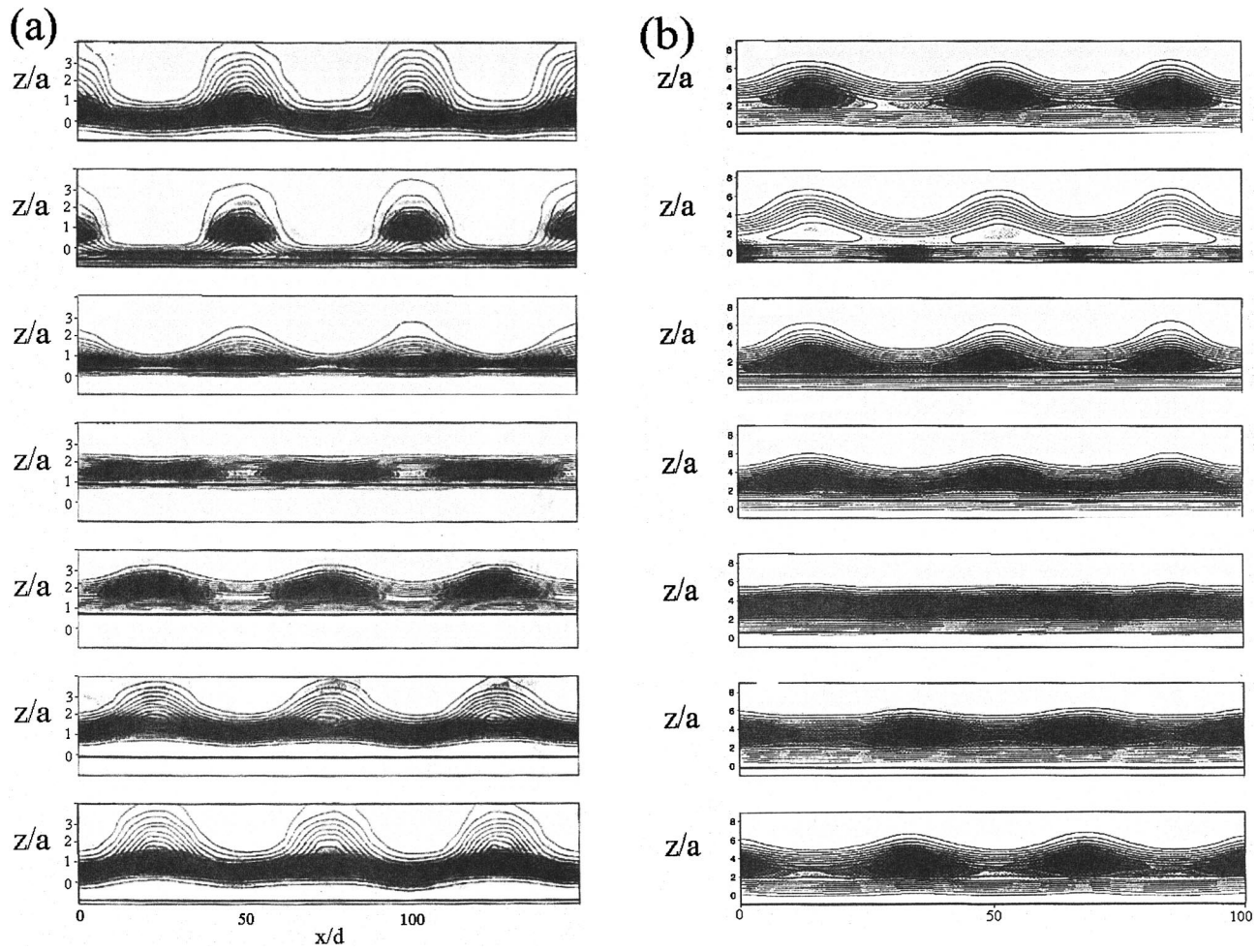

FIG. 2. Display of the pressure fields (isolines) and density fields (gray scale) for a time series over one period. The simulation parameters are $d=1$ mm and $\Gamma=3.6$. (a) $N_h=6$, $f=10$ Hz such that $Hk=0.68$; (b) $N_h=12$, $f=15$ Hz such that $Hk=1.86$.

pressure on the plate at the moment when the layer finishes its free fall and we observe indeed a regular but nonuniform distribution of pressures driving the layer. The general reason for this high pressure impact and nonuniformity is both the presence of a higher compaction state inside the peaks and a larger number of particles in the vertical direction (corresponding to the peak amplitude). As a consequence, an important momentum flux is initially localized on the plate at the peak positions. These regions of high pressure transfer large horizontal momentum to regions of low pressure. Thereafter, two horizontal energetic masses flow from the former peak positions in order to collide head on at the place where a dip was formerly present. Due to the presence of the bottom plate, this head-on collision results in an upward momentum flux. When the amplitude of the plate is at its highest point, the layer is almost flat, but the spatial distribution of extra upward momentum (i.e., with a velocity higher than the average layer velocity) will mark the place for a new peak when the layer leaves the plate again. We see that this nonuniform driving, in time and space, is *a priori* quite different from the driving mechanism in fluids (namely, a *uniform* acceleration modulation). We also noticed that, just before the free flight regime, regions where the former peaks were present and where the pressure is high are still in contact with the plate and subsequently will fall with a small initial velocity. Regions with a high upward momentum have at this instant almost no mechanical contact with the plate. This velocity difference contributes to the peak formation as well as the distortion of the layer creating the arches.

In Fig. 4, we checked that the peak amplitude p scales as $p \simeq 4a$, consistently with a previous experimental determination [10]. Here, we recall the simple scaling argument. The peak amplitude is, in first approximation, proportional to the maximum velocity difference (i.e., $\approx a\omega$) between regions of the layer before the free flight. The pattern develops during the free flight over half a period (i.e., $\approx 1/\omega$). Thus, the product of the two terms gives a scale for the vertical separation between these regions. As a consequence, the peak amplitude is proportional to the excitation amplitude. Of course, the velocity difference and the time of flight should also depend in principle on the reduced acceleration. But, interestingly, this dependence is rather weak in the conditions where the patterns develop.

IV. PATTERN WAVELENGTH SELECTION

Now we investigate the wavelength selected at a constant driving acceleration. Note that the choice of a constant acceleration is made in reference to the basic model of a single and completely inelastic block driven by a vibrating plate. In this case, the acceleration is the fundamental parameter describing the block dynamics and in particular the rates of

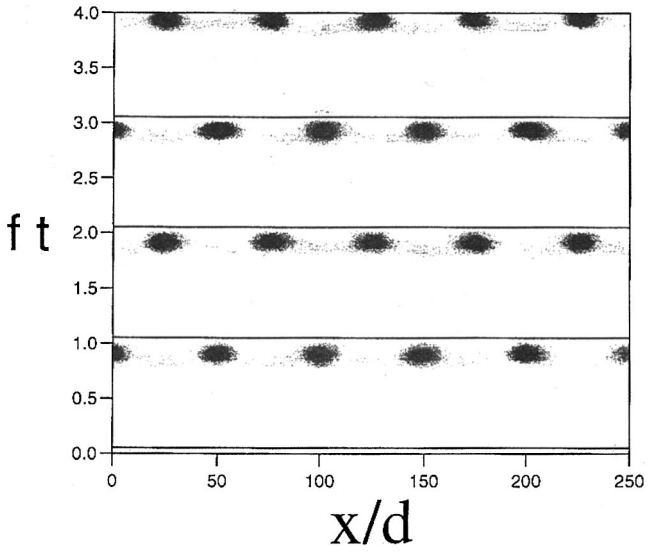

FIG. 3. Spatiotemporal diagram in arbitrary gray units of the horizontal pressure on the plate as a function of the rescaled time ft. The results were obtained for $f=15$ Hz, $\Gamma=3.6$, $d=1$ mm, and $N_h=12$ layers of grains.

collision and energy transfer (see [2] and references therein). Since the layer dissipates most of its energy on each collision with the plate, it is natural to consider in a first approximation that the center of mass will follow such a dynamics. We monitored the wavelength of the pattern, $\lambda=2\pi/k$, using the horizontal density autocorrelation function technique described in Ref. [11], which marks the presence of the peaks.

In Fig. 5, we present simulation results at $\Gamma=3.6$ where the pattern is fully developed for two layer heights $N_h=6$ and 12. The quantity ω_0^2/gk is plotted as a function of $Hk=2\pi H/\lambda$. We recall that for the Faraday instability, corresponding to the parametric excitation of gravity waves, one would get a dispersion relation (at the edge of instability) $\omega^2/4gk=\tanh(Hk)$ [30]. In this representation, we observe two different regimes: (i) at low frequencies a dispersive regime (we mean here that the wavelength depends *explicitly* on the impact frequency) such that the wavelength selected is surprisingly close to that given by the dispersion relation for gravity waves in a fluid [i.e., $\omega^2/4gk=O(1)$] and (ii) at larger frequencies a saturation regime ($\lambda=2\pi/k=$const) with a crossover depending on the layer height. Now both regimes are examined independently and computations made in a large range of bead sizes, frequencies, layer heights, and accelerations.

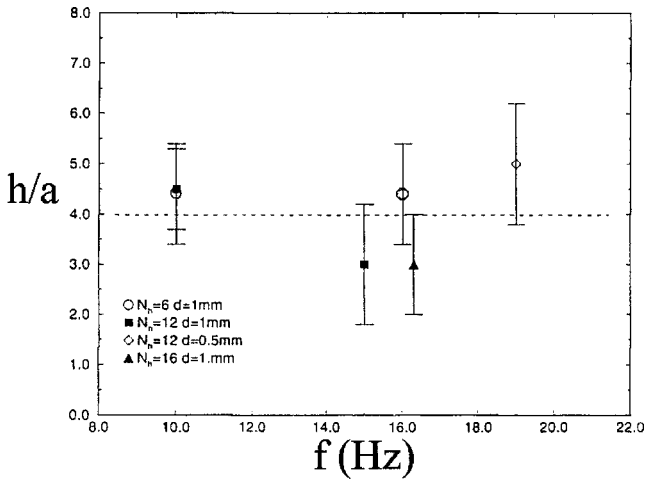

FIG. 4. Rescaled amplitude of the peaks p/a as a function of frequency f for $\Gamma=3.6$. The horizontal line is the experimental determination $p/a=4$. $N_h=6$, $d=1$ mm, (○); $N_h=12$, $d=1$ mm (■); $N_h=12$, $d=0.5$ mm (◇): $N_h=16$, $d=1$ mm (▲).

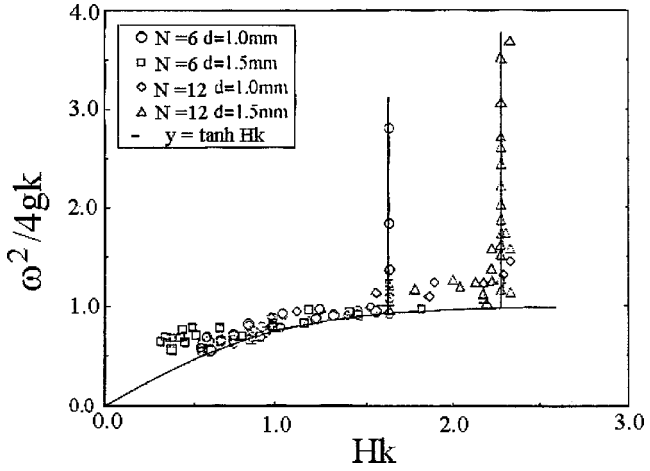

FIG. 5. Selected wavelength $\lambda=2\pi/k$ displayed in the form $\omega^2/4gk$ as a function of Hk; $\omega/2\pi$ is the driving. The continuous line is $y=\tanh x$. Plots for $N_h=6$, $d=1$ mm (○); $N_h=6$, $d=1.5$ mm (□); $N_h=12$, $d=1$ mm (◇); $N_h=12$, $d=1.5$ mm (△).

A. The dispersive regime

Simulation results for the dispersive regime are presented in Fig. 6. In this representation, we observe a collapse of the whole data set around a straight slope bounded by two extreme values: $0.25<Hk<2.8$ and $0.4<\omega_0^2/gk<1.5$. For $Hk<0.25$, we could not obtain stable patterns; the height of the peaks being so large, we obtained a vertical rupture of the layer. We simulated the pattern formation using three accelerations. We have $\Gamma=2.5$, just above the threshold, then $\Gamma=3.6$, and also $\Gamma=6.8$. In the last case, the collision frequency is just one period larger than for $\Gamma=3.6$ and thus the response is $\omega_0=\omega/4$. The data collapse is interrupted at high frequencies by wavelength saturation $\lambda_{\text{sat}}(N_h,d)$, whose values are reported in Fig. 7 (see next subsection). Note that there is still in this representation some important data scattering due, for the most part, to the difficulty of extracting a wavelength with a precision down to a few grain sizes. This is essentially the meaning of the error bars in Figs. 6(b) and 7. It can be relatively important for small wavelengths (i.e., when $Hk>1$). Within the data scattering, we could not show in this representation systematic variations of the data collapse with acceleration. The empirical best fit of the data is the straight line:

$$\omega_0^2/gk=A+BHk \tag{2}$$

[see Fig. 6(a)] with $A=0.44\ (\pm 0.02)$ and $B=0.37\ (\pm 0.01)$. We verified that these results are in reasonable agreement with the wavelength selection observed experimentally in 2D [10] and 3D [3,21] [see Fig. 6(b)]. For the 2D case, we do not recover the slight shift of the experi-

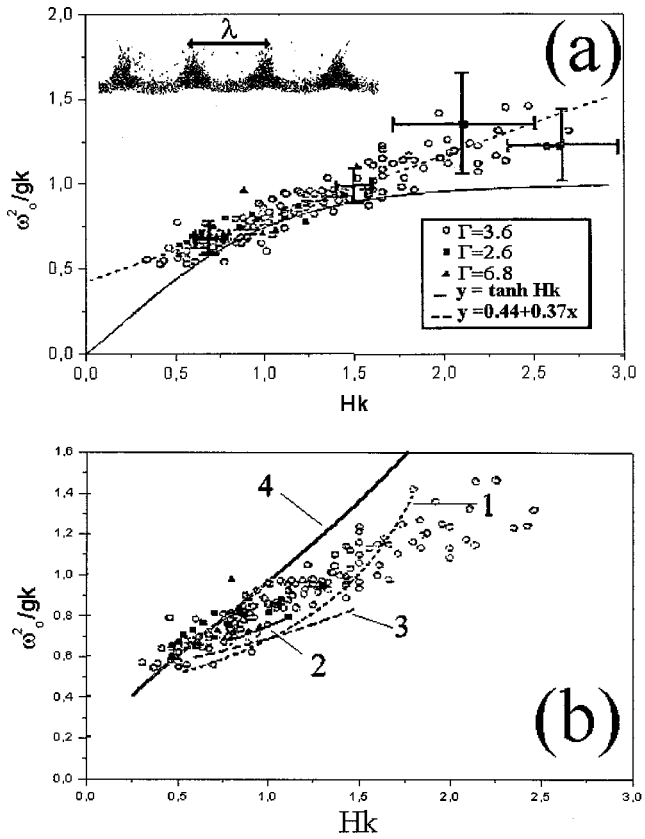

FIG. 6. Dispersive part of the selected wavelength $\lambda = 2\pi/k$ displayed in the form ω_0^2/gk as a function of Hk; $\omega_0/2\pi$ is the layer response frequency. Plots for $N_h = 6$, $d = 1$ mm (○); $N_h = 6$, $d = 1.5$ mm (□); $N_h = 12$, $d = 1$ mm (◇); $N_h = 12$, $d = 1.5$ mm (△). (a) Dispersive part for $\Gamma = 3.6$ (○); 2.6 (■); 6.8 (▲) (for many layer heights and bead diameters). The dotted line is the empirical linear best fit and crosses are typical error bars. (b) Same data but compared with other empirical fits. Line 1 is from Ref. [10] in 2D for $N_h = 6$, line 2 is from Ref. [10] in 2D for $N_h = 12$, line 3 is from Ref. [3] for $N_h = 6$ in 3D, and line 4 is from Ref. [21] in 3D.

mental dispersion relation with the number of layers (not the height) as was proposed earlier to fit the data [10]. This is possibly due to the general experimental problems in 2D, where interactions with the frontal boundaries might play a role. For the recent data set collected by Umbanhowar and Swinney [21] the proposed fit $\lambda/H = 1 + 1.1(f\sqrt{H/g})^{-1.32}$ is very close to our data in the region $HK \leqslant 1$ but seems to exhibit a slight discrepancy for $HK > 1$. In our understanding, an open question is how much the weight of the saturation regime data (which should have been removed in principle) is still influencing the empirical fit proposed by Umbanhowar and Swinney [21]. Such a spurious effect could possibly have created a systematic deviation of the fit to the upper part of the diagram as witnessed by curve 4 of Fig. 6(b).

Note that the presence of a restoring mechanism due to gravity (the peaks are collapsing on the plate) is consistent with the standard mechanical picture where the average momentum density or the mass fluxes transferred during the energy input phase ($\approx \rho V_{\text{impact}}/T$) are driven by a pressure difference on the scale of the wavelength ($\approx \Delta P/\lambda$). If we estimate that the pressure difference scales with the peak amplitude p, i.e., $\Delta P \approx \rho g p$, we obtain the balance equation,

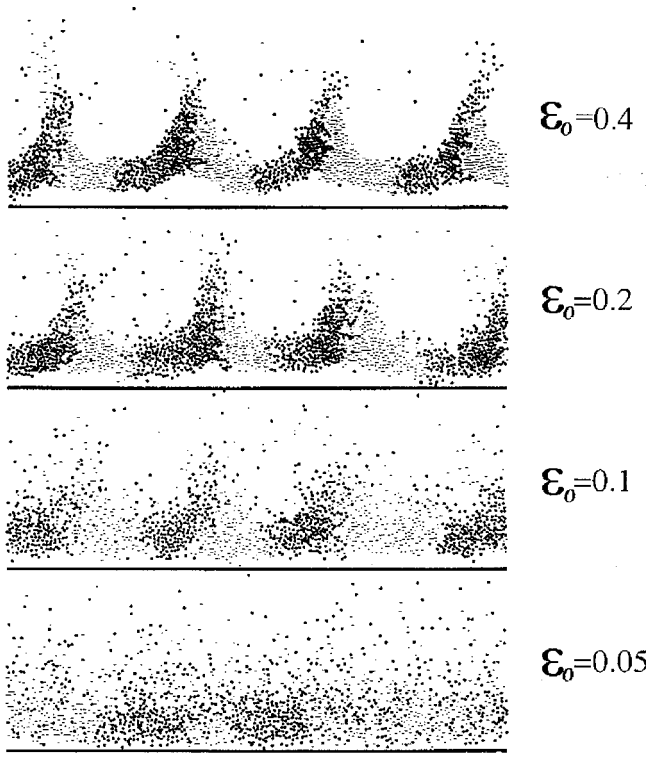

FIG. 7. Influence of dissipation on the selected pattern. The four pictures are obtained in the same conditions but for different dissipation coefficient parameters ε_0 [see Eq. (1)].

and since we also have $p \approx a$ we obtain $\rho a \omega^2 \approx \rho g a/\lambda$. This relation is a dimensional argument that could explain why we observe the limiting law for ''pure'' gravity waves $\omega_0^2/gk \rightarrow$ const at low frequencies, i.e., in the limit where $\lambda \gg H$. This relation would agree with the qualitative picture given by Melo, Ubanbovar, and Swinney [3]. But at larger frequencies (before saturation) the internal density and pressure waves play an important role as well [see Fig. 2(b)] since now the peak amplitude is small, and we propose that the limiting restoring mechanism corresponds to the limiting velocity of a shock wave caused by the impact with the bottom plate. If we estimate its velocity to be of magnitude $c \approx \sqrt{gH}$, we then propose a contribution to the dispersion relation of the type $\omega = ck$ and thus $\omega^2/gk \approx kH$. As a consequence, in our understanding, the selection mechanism is a complex interplay between the possibilities of global deformation of the granular layer (i.e., arching and peak amplitude) and the internal dynamics of pressure/density waves due to the vertical impact.

Furthermore, in reference to the 3D patterns, we notice immediately that, in our framework of interpretation, the transition from square to stripe occurs when both mechanisms (gravity and pressure waves) are of the same magnitude, i.e., $A \cong BHk$. This corresponds more precisely, following Ref. [12], to $\omega_0^2/gk \simeq 0.96$ and $Hk \simeq 1.4$. It is thus similar to the criterion proposed empirically by Bizon *et al.* [12] to predict this transition, i.e., $f^* = f\sqrt{H/g} \cong 0.37$. But interestingly, for higher acceleration around $\Gamma = 6$, by applying our criterion ($\omega_0^2/gk \simeq 0.96 \Rightarrow Hk \simeq 1.4$), we get a prediction for the transition that is $f^* = f\sqrt{H/g} \cong 0.71$. This last prediction is really in close agreement with the experimental finding of [3]. In this last situation, where $\omega_0 = \omega/4$, the tran-

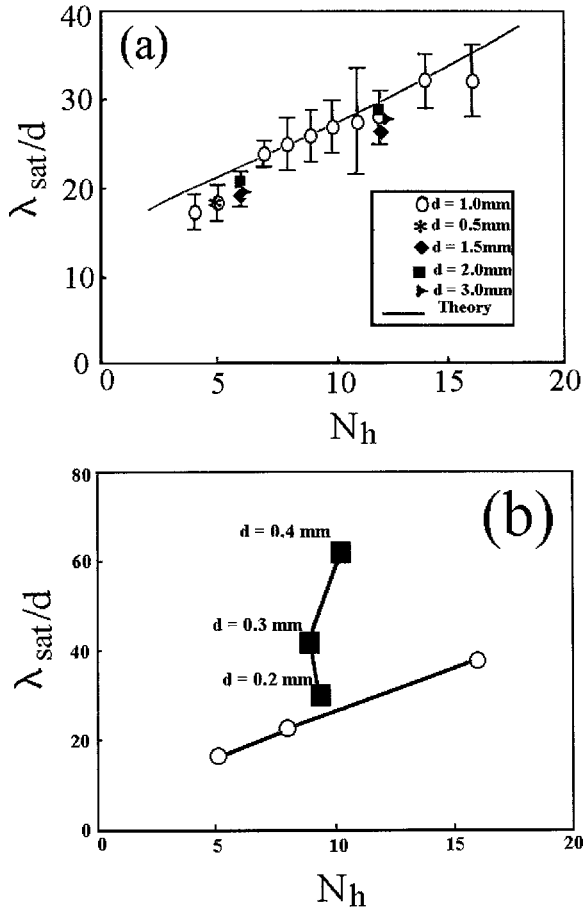

FIG. 8. Saturation regime of the selected wavelength: λ_{sat}/d as a function of the number of layers N_h. (a) Numerical results for $d=0.5$ (*), 1 (○), 1.5 (◆), 2 (■), and 3 mm (▲); the straight line is the theoretical prediction (see text). (b) Experimental data extracted from Fig. 2 of Ref. [10] (○) and Fig. 3 of Ref. [3] (■).

sition is observed for $0.6<f\sqrt{H/g}\lesssim 0.8$.

In Fig. 7, we illustrate the fact that, in this regime, the selection pattern does not depend on the detailed dissipative character of the granular collisions. It is essentially due to large scale momentum transfer. We display a picture of the waves for increasing restitution coefficient (decreasing dissipation). The selected wavelength stays constant but the system is moving progressively toward an extended fluidization when $\varepsilon_0\rightarrow 1$.

As a consequence, in the dispersive regime, the physical picture we propose is to the best of our knowledge very consistent with all the experimental and numerical results available.

B. The saturation regime

Now, we focus on the saturating regime obtained at high frequencies. We measure the saturation wavelength λ_{sat} for various pairs of parameters (N_h,d). From our measurements [see Fig. 8(a)], we observe a roughly linear increase of this selected length with the number of layers.

In Fig. 8(b), we report some experimental data taken from Ref. [10] in 2D and extracted from Ref. [3] in 3D that show saturation. The 2D case was obtained with a constant bead size (1.5 mm aluminum beads). We actually have a clear

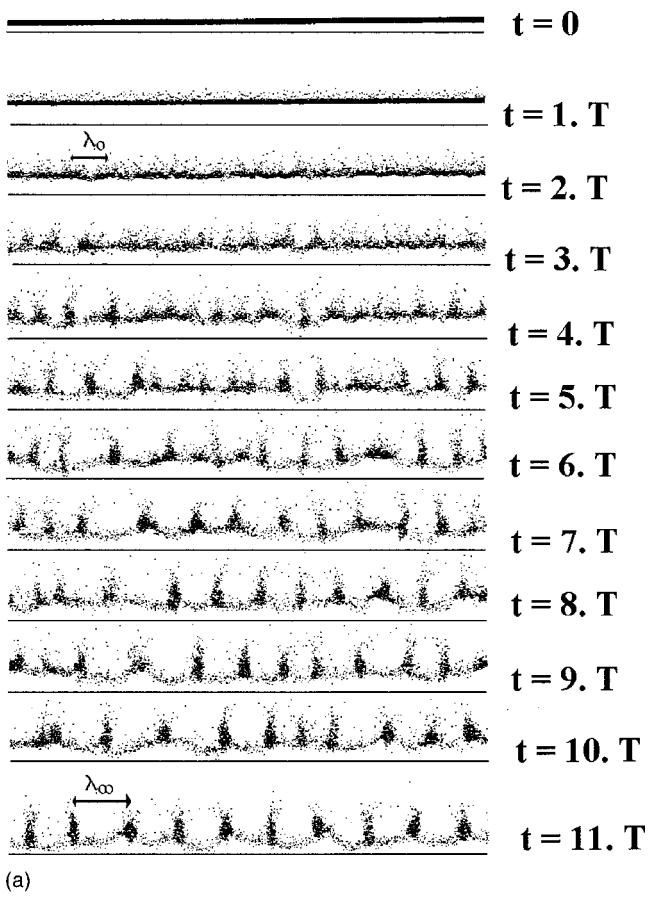

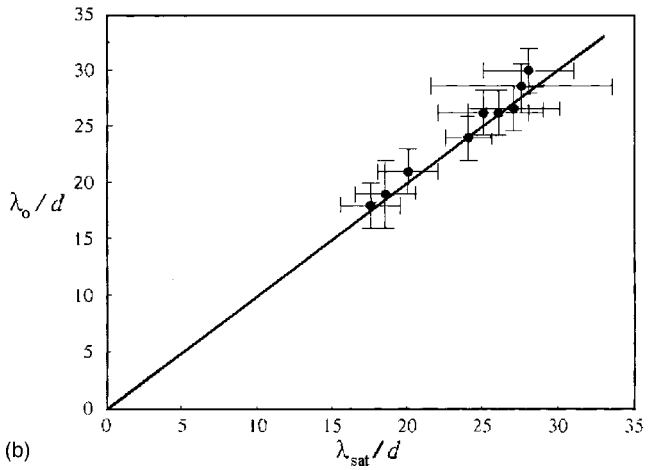

FIG. 9. Time development of patterns in a numerical simulation performed in the dispersive regime. (a) Is a visualization of the wavelength growth. (b) Shows the early selected wavelength λ_0 (after the first two collisions) for a simulation in the dispersive regime as a function of the saturation wavelength λ_{sat} obtained at higher frequencies and for a constant acceleration $\Gamma=3.6$.

increase of the saturation wavelength value with the layer height. In the 3D case the layer height is almost the same for the three cases reported. The bead size is changed. Thus, we see that the grain size effect on the saturation wavelength is quite important.

By monitoring the development of the pattern in the *dispersive regime,* we realized that at the first and second impact a typical wavelength λ_0 is already selected characteriz-

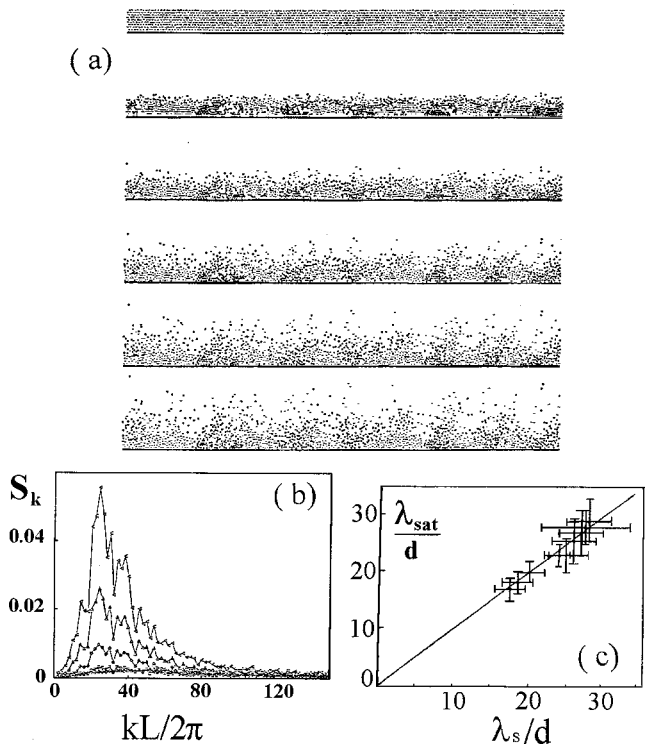

FIG. 10. Layer instability after impact at a constant velocity (no gravity). (a) Visualization of the pattern formation after impact. (b) Time evolution of the horizontal density structure factor S_k. From bottom to top, $t=0.03$, 0.06, 0.09, 0.12, and 0.15 s. (c) Saturation wavelength λ_{sat} as a function of the selected wavelength λ_s for the same number of layers N_h.

ing a modulation of the horizontal density [see Fig. 9(a)]. At long times, we get the expected dispersive wavelength λ_∞ in agreement with relation (2). This initial length $\lambda_0(N_h,d)$ corresponds *exactly* to the saturation length $\lambda_{sat}(N_h,d)$ that we obtain at steady state when the frequency is increased (keeping a constant acceleration) [see Fig. 9(b)].

Now we relate this early pattern selection to the general issue of a granular stripe instability, initially at rest and in the absence of gravity [see Fig. 10(a)]. We calculate the horizontal density distribution $\sigma(x)=\int\rho(x,z)dz$. The power spectrum of this distribution $S_k=\langle\tilde{\sigma}_k\tilde{\sigma}_k^*\rangle$ is monitored as a function of time [Fig. 10(b)]. We observe a band of unstable modes with the fastest growing wavelength characterized by the wave number $k_s=2\pi/\lambda_s$. In Fig. 10(c), we report this selected wavelength λ_s as a function of the saturation wavelength for various sets of experiments, $\lambda_{sat}(N_h,d)$. We observe that $\lambda_s\simeq\lambda_0\simeq\lambda_{sat}(N_h,d)$. This is why, in the following, we report results of a systematic study on the pattern created by the impact of a moving plate on a layer of grains.

V. STUDY OF IMPACTED LAYERS OF GRAINS

A. Constant restitution coefficient

In the following, we report results on the internal dynamics of an impacted layer of dissipative grains in 2D. A more complete study of this issue was done by Labous [31] and will be reported elsewhere [32]. For the present purpose, we present only the results relevant to a discussion of the pattern wavelength selection of the ''granular Faraday'' waves. The

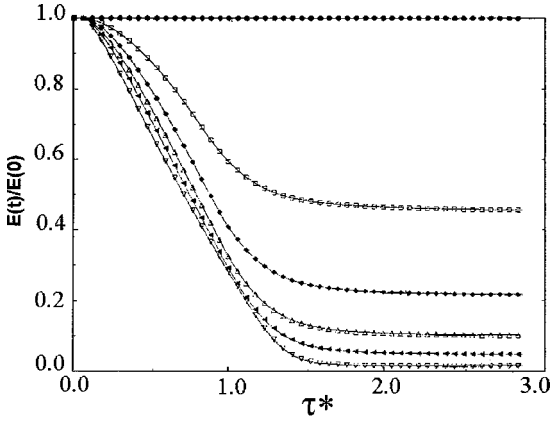

FIG. 11. Layer kinetic energy $E(t)$ rescaled by the initial kinetic energy E_0 before impact as a function of rescaled time $\tau^*=t/t_{coll}$. The layer height is $N_h=40$ beads. From top to bottom, $\varepsilon=1$, 0.99, 0.98, 0.97, 0.96, and 0.94.

waves we are interested in are compaction/dilation waves for hard spheres. The problem of energy and momentum transfer due to a shock with a plate has been studied analytically and by numerical simulations for 1D columns of hard and dissipative grains [25,33]. Note that these waves may be quite different from those obtained in the case of columns made of soft particles [34,29,35,36] where the detailed value of the interparticle potential plays a central role.

As a first step, the study is made with values of the restitution coefficient independent of the impact velocities. We simulate a layer of N_h grains (vertical direction) initially prepared in a quasitriangular array but with a typical separation between grains around s_0, the value being taken at random around this mean. The values of s_0 we are interested in are such that $s_0/d\ll 1$ (typically s_0/d ranging between 0.01 and 0.1). In this compacted limit, the exact value of s_0/d does not matter much. The grains have an initial velocity $-U_0$, i.e., pointing toward the plate. We identify two important phases as a result of the impact.

(i) Just after the impact, an upward compression wave and a downward dilation wave cross the layer vertically at very large speed $c\approx U_0 d/s_0$. These waves cross the system on a time scale $t_{coll}\simeq N_h s_0/U_0$. They do not cause global distortion of the layer but are extremely dissipative. To illustrate this point, we display in Fig. 11 the time evolution of the kinetic energy as a function of the rescaled time t/t_{coll}, for a layer of $N_h=40$ grains and several different restitution coefficients. We see that for $(1-\varepsilon)N_h\gtrsim 2$ we already have an almost complete dissipation of the energy, as already noted by Luding, Herrmann, and Blumen [37].

(ii) After the passage of those waves an expansion of the layer follows, characterized by a vertical increasing velocity gradient $G=\partial V(z)/\partial z>0$, and subsequently, after a time t_{exp}, the layer will lose contact with the plate to expand in vacuum. The time scale to reach this expansion is such that $t_{exp}G=O(1)$ [see Fig. 12(a)]. A systematic study of the scaling behavior of this gradient shows that we have

$$G\approx\frac{U_0}{H}\exp[-\xi(N_h-1)(1-\varepsilon)] \tag{3}$$

with $\xi\simeq 1.1\pm 0.15$ [see Fig. 12(b)].

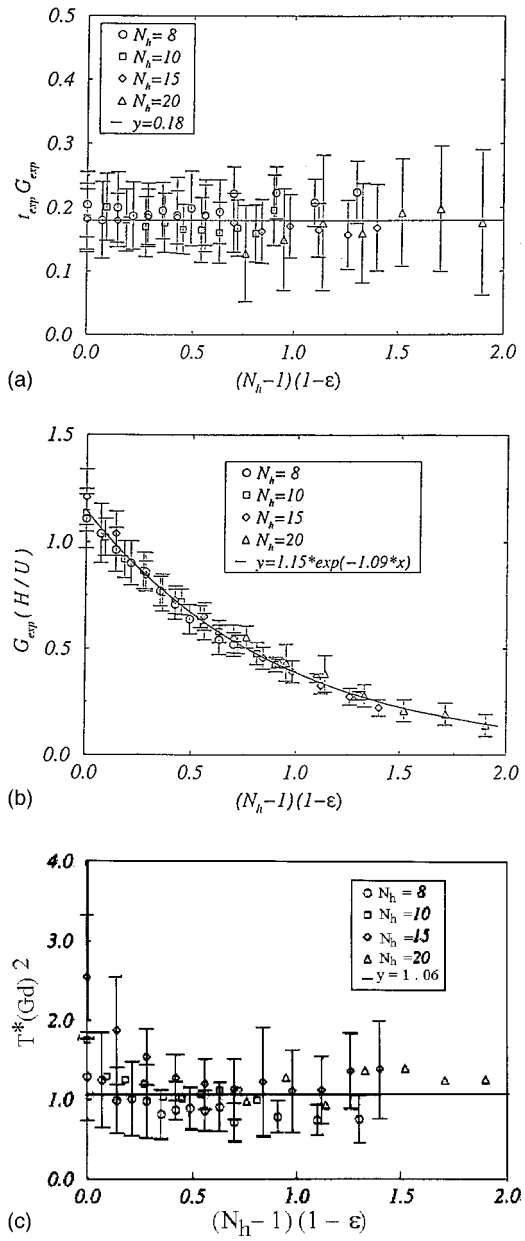

FIG. 12. Internal dynamics of an impacted layer of grains. (a) $t_{\exp}$, the time to reach the expansion phase, rescaled by the velocity gradient G as a function of the parameter $X=(1-\varepsilon)(N_h-1)$. (b) Log-normal plot of the rescaled velocity gradient GH/U_0 as a function of X. (c) Temperature T^* at the onset of the expansion phase rescaled by the velocity gradient $T^*/(Gd)^2$ as a function of X.

At the beginning of the expansion phase, the layer exhibits a quasiuniform agitation characterized by a temperature T^*. A systematic study of this temperature (taken just above the bottom plate) shows that $T^* \simeq (Gd)^2$, i.e.,

$$T^* = C_1 \frac{U_0^2}{H^2} d^2 \exp[-2\xi(N_h-1)(1-\varepsilon)] \tag{4}$$

with $C_1 = 1.1 \pm 0.1$. [see Fig. 12(c)] During the expansion phase, the layer is unstable and a wavelength characterizing a density modulation in the horizontal direction shows up. In Fig. 13(a), we represent the value of this wavelength for

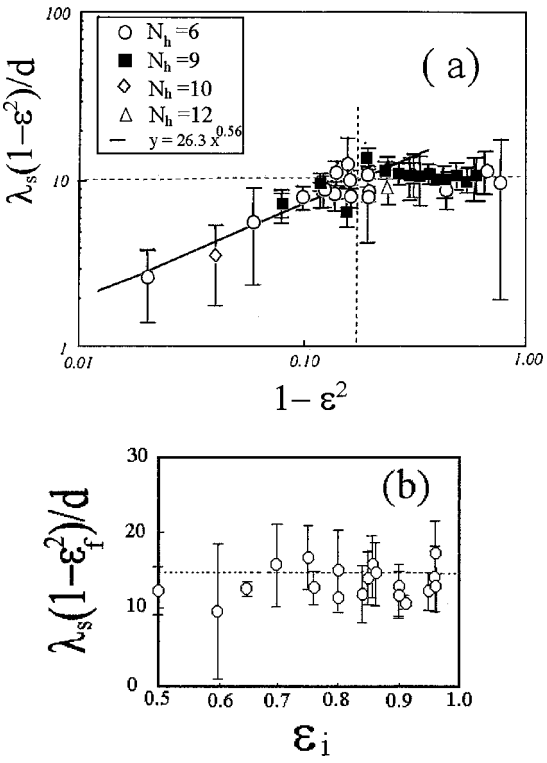

FIG. 13. Dependence of the selected wavelength λ_s on dissipation for an impacted layer. (a) Simulation results for a constant restitution coefficient ε, rescaled selected wavelength $\lambda_s(1-\varepsilon^2)/d$ plotted as a function of the dissipation $(1-\varepsilon^2)$. (b) Simulation results for a velocity dependent restitution coefficient; the rescaled wavelength $\lambda_s(1-\varepsilon_f^2)^{1/2}/d$ is plotted as a function of the initial restitution ε_i. The layer heights used are $N_h=6,8,10,12$; the horizontal dotted line is $y=14.7$.

different constant coefficients of restitution ε (we recall that now ε is independent of the collision velocities). We can distinguish two limiting regimes such that

$$\lambda_s/d \approx 1/(1-\varepsilon^2)^{\beta}, \tag{5}$$

where $\beta \simeq 1$ in the strong dissipation regime [i.e., $1-\varepsilon = O(1)$] and $\beta = 0.44 \pm 0.08 \simeq 0.5$ in the weak dissipation limit (i.e., $1-\varepsilon \to 0$). Note that such scaling relations between a structural length scale and a restitution coefficient have already been identified in the case of freely evolving granular gases. The scaling with $\beta=1$ is naturally occurring in the formation of 1D structures and clusters with long lasting multiple contacts [25] and the scaling with $\beta \simeq 0.5$ is naturally occurring at the onset of a structural instability in weakly dissipative granular gases described by dissipative hydrodynamics [38]. Importantly, for constant restitution coefficients, these regimes show a selected wavelength value λ_s that is *independent* of the number of layers N_h.

B. Velocity dependent restitution coefficient

Now, we pursue the same study but with a restitution coefficient depending on the collision velocity. We have in the early stage an impact with a layer moving at a constant velocity $-U_i$, and therefore, a typical initial restitution coefficient $\varepsilon_i = 1-\varepsilon_0(U_i/u^*)^{\alpha}$ (for our simulations we use α

$=\frac{1}{5}$). But after a large number of impacts, the average kinetic energy of the layer is decreased and we get a typical final restitution coefficient $\varepsilon_f = 1-\varepsilon_0(U_f/u^*)^\alpha$ characterized by a typical collision velocity U_f just before the expansion phase.

Therefore, using a relation setting the scale of the typical collision velocity to the order of the agitation at the onset of the expansion phase, i.e.,

$$T^* \equiv U_f^2, \tag{6}$$

we estimate the final restitution coefficient using the relation

$$\frac{1-\varepsilon_f}{1-\varepsilon_i} = (U_f/U_i)^\alpha. \tag{7}$$

Now we report the results of a series of numerical simulations with varying layer heights and initial restitution coefficients. For each numerical simulation, we determine the final restitution coefficient ε_f according to relation (7) and we measure the selected wavelength λ_s. In Fig. 13(b) we plot the rescaled wavelength $\lambda_s(1-\varepsilon_f^2)^{1/2}/d$ as a function of the initial restitution coefficient ε_i. Thus we estimate the scaling relation

$$\lambda_s/d = \frac{C}{(1-\varepsilon_f^2)^\beta} \tag{8}$$

with $\beta \simeq 0.5$ and $C \simeq 15 \pm 2$. Now the dependence of the selected wavelength on the number of layers is implicitly contained in the value of the final restitution coefficient since this last relation depends on the final temperature obtained from relation (4). The $\beta = \frac{1}{2}$ exponent indicates that the selection mechanism for the wavelength rather corresponds to the weak dissipation limit we identified previously (although the dissipation was quite high initially).

C. The saturation regime revisited

As a consequence of putting together Eqs. (5)–(8) we get a mean-field theoretical prediction for the saturation wavelength. The value of λ_s obtained numerically by solving these relations is displayed in Fig. 8(a). In the limit $\varepsilon_i \to 1$, we obtain an asymptotic formula for the selected wavelength for any α and N_h:

$$\lambda_s/d \approx \frac{1}{(1-\varepsilon_i)^{1/2}} N_h^{\alpha/2} \exp\left[\frac{\alpha}{2}\xi(N_h-1)(1-\varepsilon_i)\right]. \tag{9}$$

We realize here that the exponential growth of the selected length with the number of layers is damped by the weak value of the coefficient α characterizing the velocity dependence of the dissipation. Thus, the two antagonistic effects give an approximately linear increase of the wavelength. As a consequence, the presence of an intrinsic instability due to the dissipative character of the granular collisions prevents the selected wavelength from decreasing (when the frequency is increased) to a value smaller than this intrinsic dissipative length. The vibrations are here only to sustain the motion due to this imposed density modulation and drive the dynamics such that larger densities in the layer create larger agitations and thus larger pressures. As a consequence, a horizontal flow develops toward lower pressure regions and the alternative horizontal motion is sustained at the pace of the vertical impacts with the plate. The dependence of the saturated wavelength on the number of layers is related to the dissipation properties of the grains, which depend on the typical collision velocities between two grains. Also, in the case of real systems the restitution coefficient on binary collision may vary with the grain size (see [24]). For example, in the case of the Herz-Kuwabara-Kono model, one would get $\varepsilon_0 \approx d^{-1/2}$. Thus, it is clear that a systematic study of the variation this selected saturation wavelength with the bead size and the layer height could possibly shed some light on the real dissipation mechanisms taking place at the granular level for a dense assembly of vibrated grains.

VI. CONCLUSION

In conclusion, we presented a numerical study of a pattern-forming instability occurring in a 2D vibrated layer of dissipative grains. We focused on mechanisms leading to the formation of stationary oscillating surface peaks that are separated by a well defined wavelength $\lambda = 2\pi/k$. We identified two distinct regimes. The first regime (dispersive) corresponds to a periodic excitation of the layer where the gravity restoring force plays an important role in competition with internal density and pressure waves created by repeated impacts with the bottom plate. The dispersion relation is such that we have in general a relation of the type $\omega_0^2/4gk = O(1)$ with a value smaller for thin channels and larger for thick channels (sizes being compared to the selected wavelength). The frequency $f_0 = \omega_0/2\pi$ is the pattern response frequency. We propose an empirical relation $\omega_0^2/4gk = A + BHk$ with values of A and B almost independent of the driving acceleration. The agreement with available experimental data is quite satisfactory. At larger frequencies (acceleration being constant) this dispersion relation is interrupted by a saturation regime where the wavelength is now independent of the frequency. We show how this wavelength selection is related to an instability occurring spontaneously in dissipative gases We also stress the influence of the detailed microscopic dissipation laws affecting the values of the selected wavelength.

ACKNOWLEDGMENT

We are grateful to Dr. S. Luding for many interesting discussions.

[1] H. M. Jaeger, S. R. Nagel, and R. P. Behringer, Rev. Mod. Phys. **68**, 1259 (1996).

[2] E. Clément, in *Physics of Dry Granular Media*, edited by H. J. Herrmann, J.-P. Hovi, and S. Luding (Kluwer, Dordrecht, 1998), p. 585.

[3] F. Melo, P. Ubanhovar, and H. Swinney, Phys. Rev. Lett. **72**,

172 (1994); **75**, 3838 (1995).
[4] T. H. Metcalf, J. B. Knight, and H. M. Jaeger, Physica A **236**, 202 (1997).
[5] S. Fauve, S. Douady, and C. Laroche, J. Phys. (Paris) **50**, Suppl. 3 187 (1989).
[6] M. Faraday, Philos. Trans. R. Soc. London **121**, 299 (1831).
[7] M. C. Cross and P. C. Hohenberg, Rev. Mod. Phys. **65**, 851 (1993).
[8] P. Umbanhowar, F. Melo, and H. Swinney, Nature (London) **382**, 793 (1996).
[9] J. R. de Bruyn, C. Bizon, M. D. Shattuck, D. Goldman, J. B. Swift, and Harry L. Swinney, Phys. Rev. Lett. **81**, 1421 (1998).
[10] E. Clément, L. Vanel, J. Duran, and J. Rajchenbach, Phys. Rev. E **53**, 2972 (1996).
[11] S. Luding, E. Clément, J. Rajchenbach, and J. Duran, Europhys. Lett. **36**, 247 (1996).
[12] C. Bizon, M. D. Shatuck, J. B. Swift, W. D. McCormick, and H. Swinney, Phys. Rev. Lett. **80**, 57 (1998).
[13] K. M. Aoki and T. Akiyama, Phys. Rev. Lett. **77**, 4166 (1996).
[14] T. Shinbrot, Nature (London) **389**, 574 (1997).
[15] L. S. Tsimring and I. S. Aronson, Phys. Rev. Lett. **79**, 213 (1997).
[16] D. H. Rothman, Phys. Rev. E **57**, 1239 (1998).
[17] E. Cerda, F. Melo, and S. Rica, Phys. Rev. Lett. **79**, 4570 (1997).
[18] S. C. Venkataramani and E. Ott, Phys. Rev. Lett. **80**, 3495 (1998).
[19] J. Eggers and H. Riecke, Phys. Rev. E **59**, 4476 (1999).
[20] C. Bizon, M. D. Shattuck, and J. B. Swift, Phys. Rev. E **60**, 7210 (1999).
[21] P. Umbanhowar and H. Swinney, Physica A **274**, 345 (2000).
[22] E. Clément and L. Labous, in *Granular Gases*, edited by S. Luding and T. Poeschel (Springer-Verlag, Berlin, in press).
[23] W. Goldsmith, *Impact, the Theory and Physical Behavior of Colliding Solids* (Arnord, London, 1960); O. Walton *et al.*, J. Rheol. **30**, 949 (1983). S. F. Foerster *et al.*, Phys. Fluids **6**, 1108 (1994).
[24] L. Labous *et al.*, Phys. Rev. E **56**, 5717 (1997).
[25] B. Bernu and R. Mazighi, J. Phys. A **23**, 5745 (1990); S. MacNamara and W. R. Young, Phys. Fluids A **5**, 34 (1993).
[26] G. Kuwabara and K. Kono, Jpn. J. Appl. Phys., Part 1 **26**, 1230 (1987).
[27] S. Luding and S. McNamara, Granular Matter **1**, 113 (1998).
[28] B. D. Lubaschevsky, J. Comput. Phys. **94**, 255 (1991).
[29] S. Luding, E. Clement, A. Blumen, J. Rajchenbach, and J. Duran, Phys. Rev. E **50**, 4113 (1994).
[30] L. D. Landau and E. Lifschitz, *Fluid Mechanics* (Pergamon, London, 1963).
[31] L. Labous, Ph.D. dissertation, Université Paris VI, 1998.
[32] L. Labous and E. Clément (unpublished).
[33] A. Goldshtein and M. Shapiro, J. Fluid Mech. **282**, 75 (1995); A. Goldshtein, M. Shapiro, and C. Gutfinger, *ibid.* **316**, 29 (1996); **327**, 117 (1996).
[34] V. Nesterenko, J. Appl. Mech. Tech. Phys. **5**, 733 (1983); J. Phys. IV **4**, C8-729 (1994).
[35] C. Coste, E. Falcon, and S. Fauve, Phys. Rev. E **56**, 6104 (1997).
[36] S. Sen *et al.*, Phys. Rev. E **57**, 2386 (1998).
[37] S. Luding, H. Herrmann, and A. Blumen, Phys. Rev. E **50**, 3100 (1994).
[38] I. Goldhirsch and G. Zanetti, Phys. Rev. Lett. **70**, 1619 (1993); S. MacNamara and W. R. Young, Phys. Rev. E **50**, R28 (1994).